Control System Modeling for the Thirty Meter Telescope Primary Mirror

Douglas G. MacMynowski[a], Peter M. Thompson[b], J. Chris Shelton[c], Lewis C. Roberts, Jr.[c], M. Mark Colavita[c] and Mark J. Sirota[d]

[a]Control & Dynamical Systems, California Institute of Technology, Pasadena CA 91125
[b]Systems Technology, Inc., Hawthorne, CA 90250
[c]Jet Propulsion Laboratory, California Institute of Technology, Pasadena, CA 91109
[d]Thirty Meter Telescope Project, Pasadena, CA 91125

ABSTRACT

The Thirty Meter Telescope primary mirror is composed of 492 segments that are controlled to high precision in the presence of wind and vibration disturbances, despite the interaction with structural dynamics. The higher bandwidth and larger number of segments compared with the Keck telescopes requires greater attention to modeling to ensure success. We focus here on the development and validation of a suite of quasi-static and dynamic modeling tools required to support the design process, including robustness verification, performance estimation, and requirements flowdown. Models are used to predict the dynamic response due to wind and vibration disturbances, estimate achievable bandwidth in the presence of control-structure-interaction (CSI) and uncertainty in the interaction matrix, and simulate and analyze control algorithms and strategies, e.g. for control of focus-mode, and sensor calibration. Representative results illustrate TMT performance scaling with parameters, but the emphasis is on the modeling framework itself.

Keywords: Extremely Large Telescopes, Control Systems, Uncertainty, Dynamics

1. INTRODUCTION

The primary mirror (M1) of the Thirty Meter Telescope (TMT) is composed of 492 hexagonal segments, with the "out-of-plane" degrees of freedom controlled by the primary mirror control system (M1CS). The control approach is broadly similar to that used at the Keck Observatories,[1,2] with feedback from edge sensors used to control position actuators on each segment. However, the problem is more challenging because of the greater number of segments, sensors and actuators, higher desired control bandwidth, and stringent performance goals. Models are essential for estimating performance, making design choices, and flowing down requirements to other subsystems. The focus here is to summarize these modeling tools. Earlier analyses have been described in [3–5] and similar analyses for the European ELT in [6].

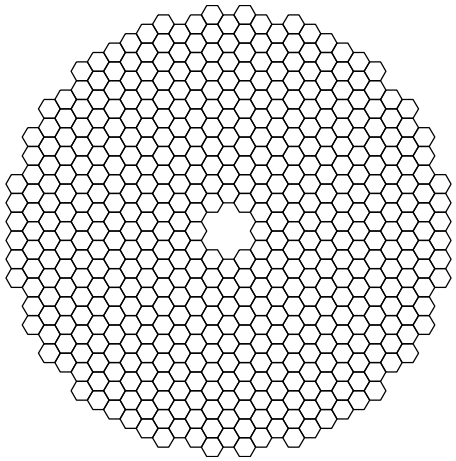

Figure 1. The primary mirror of TMT has 492 segments, each with 3 actuators, and 2 sensors on each inter-segment edge, for a total of 1476 actuators and 2772 sensors.

A brief overview of the control system and some of its features is relevant in order to put modeling goals and results into context. Each segment will have 3 "soft" voice-coil actuators, stiffened with a relatively high-bandwidth servo loop using collocated encoder feedback. Hard actuators (e.g. piezoelectric) were also considered. Differential capacitive sensors between neighbouring segments measure relative edge height discontinuity, and are also sensitive to the dihedral angle between segments; without this dihedral sensitivity, "focus-mode" would be unobservable in addition to global piston, tip and tilt. (Focus-mode corresponds to uniform dihedral change for all segments, resulting in a change in M1 focus and some wavefront scalloping due to the resulting mismatch between M1 and segment radii of curvature). The dihedral sensitivity is quantified in terms of the effective moment arm L_{eff}. The non-interlocking sensor geometry at TMT simplifies segment exchange but results in reduced L_{eff} compared to Keck; combined with the larger number of segments and sensors this makes focus-mode estimation more sensitive to sensor noise and drift, and to uncertainty in the interaction matrix between actuator motion and sensor response. The desired

Integrated Modeling of Complex Optomechanical Systems, edited by Torben Andersen, Anita Enmark,
Proc. of SPIE Vol. 8336, 83360R · © 2011 SPIE · CCC code: 0277-786X/11/$18 · doi: 10.1117/12.914941

set-point for the sensors is determined every 2–4 weeks with optical wavefront information using the Alignment and Phasing System (APS).[7] Sensor installation errors result in some cross-sensitivity to gap and shear motions between neighbouring segments; the gaps are also measured, and shear (imperfectly) estimated, and this used together with APS information to calibrate out the cross-sensitivity. In addition to the quasi-static gravity and thermal deformations controlled at Keck, M1CS at TMT will provide some reduction of the response to wind turbulence forces over M1. Vibration due to equipment is at too high a frequency for M1CS to attenuate but also needs to be modeled since the actuator type and design affect the response. The increased bandwidth required to compensate for some of the wind loads requires more careful attention to control-structure interaction (CSI) with the structural dynamics of the telescope than was required for Keck,[2] and needs to be considered for both the local actuator servo loops and the edge-sensor global feedback loop. M1CS robustness also requires attention to interaction-matrix uncertainty.

Modeling has been an esential component in design decisions. M1CS modeling has enabled TMT to push the control bandwidth significantly higher than at Keck while remaining robust to uncertainty. The higher bandwidth allows higher wind speeds across the primary mirror for thermal management of dome and mirror seeing. The trade-off between hard and soft actuators was based largely on modeling the respective achievable wind and vibration performance[3]; the sensor downselect was also informed by modeling. Different sensing options have been considered for controlling focus mode. Subsystem requirements influenced by M1CS modeling include mirror subcell structural stiffness (structural dynamics optimization is in progress), sensor L_{eff}, installation tolerances, gain stability, and drift.

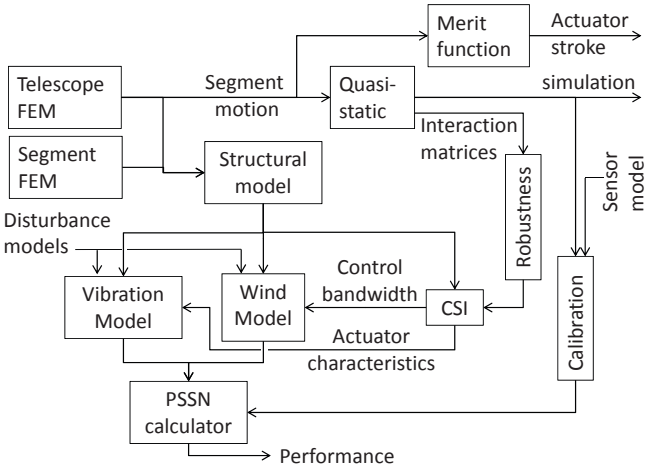

Figure 2. Modeling tools used in M1CS design and performance analysis, and the information flow between them. The seeing-limited PSSN metric is shown; model output is also evaluated with AO simulations.

Error budget performance requirements associated with M1CS include actuator and sensor noise,[8] quasi-static sensor drift effects and sensor calibration residuals, and residual uncorrected dynamic segment motion due to both wind loads and vibration. The residual segment piston/tip/tilt due to gravity and thermal deformations will be negligible. TMT will achieve excellent image quality for both seeing-limited and adaptive-optics (AO) modes of operation. The former is evaluated using the normalized point-source sensitivity (PSSN).[9] For M1CS, AO performance is typically met when seeing-limited performance is met, and for simplicity only the PSSN requirements are quoted here.

To support the design of M1CS and related subsystems, modeling must therefore:

- Simulate the overall control algorithm to verify performance, including the incorporation of optical information both in real-time and from APS, and managing the unobservable degrees of freedom,
- Simulate the sensor calibration algorithm and the resulting performance,
- Support design decisions regarding control of focus mode,
- Evaluate robustness to uncertainty in the interaction-matrix that relates sensor response to actuator motion,
- Determine the achievable bandwidth for both the actuator servo and the global (edge-sensor feedback) control loops, through modeling the interaction between the control and the structural dynamics,
- Compute the dynamic response to unsteady wind turbulence across M1,
- Compute the dynamic response to equipment and micro-seismic vibration disturbances.

The first two of these require only a quasi-static model, while the rest require varying degrees of fidelity of dynamic modeling. The basic philosophy taken here is to develop models appropriate to address specific required questions, and not to develop a single model that can answer all questions. Quasi-static modeling tools are described in Section 2, and dynamic tools in Sections 3 and 4. Relationships between the various tools are shown in Fig. 2.

2. QUASI-STEADY TOOLS

2.1. Overall simulation

The overall TMT M1CS simulation, shown in Fig. 3, was created to study the complex interaction of all of the quasi-static M1 control elements, including real-time optical feedback from either the on-instrument wavefront sensor (OIWFS) or AO, APS calibration runs, action of segment warping harnesses in addition to the segment piston/tip/tilt control, control of unobservable global piston/tip/tilt, and the calibration algorithm that compensates for changes in desired edge-sensor offset with in-plane motion. In addition to providing a simulation to verify algorithm behaviour, the modeling framework generates sensor/actuator interaction matrices that are inputs to several other analyses. Uncertainty and variation in the interaction-matrix will be discussed in Sec. 2.3, and the variation in the desired sensor set-point requires calibration discussed in Sec. 2.2.

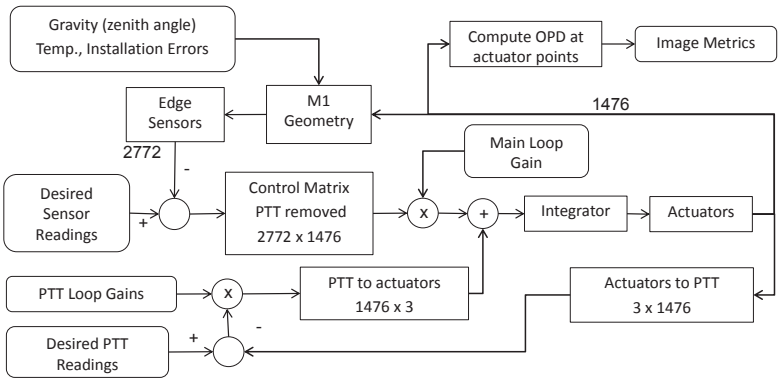

Figure 3. Quasi-static control simulation (structural dynamic effects are included in other modeling tools). The desired sensor readings are obtained from a detailed model of APS performance. The edge-sensor model includes sensor L_{eff} dependence on inter-segment gap, and sensor cross-axis sensitivity due to installation errors. The M1 geometry includes variation in segment in-plane locations due to segment installation errors, zenith angle, and temperature.

In-plane segment motion results in (i) a direct optical consequence due to the segments not having the correct curvature for their current location and orientation, (ii) a sensor response to segment clocking even for ideal sensors, due to the inter-segment height discontinuity that results from the different radial and sagittal radii of curvature, and (iii) a non-zero sensor response that results from gap and shear at the segment location; this cross-axis sensitivity is inevitable since perfect sensor installation is not practical. The latter two effects would result in an M1CS response, but can be calibrated out. Analysis uses the "full" interaction matrix that relates both in-plane and out-of-plane motion to the height, gap, and shear at the edge sensor locations; the model outputs this as a function of the detailed geometry.

Several aspects of the sensor response need to be modeled in more detail than the interaction matrix formulae in [8]. First is to use the correct non-spherical M1 optical prescription, which also results in segments that are not quite regular hexagons. The in-plane segment locations vary due to segment installation errors, zenith angle, and temperature; these affect the inter-segment gaps and shears and hence sensor response. The simulation takes as input the results of finite element analysis of gravity and thermal deformations. Note that the sensor output is the sum of the relative inter-segment height plus L_{eff} times the dihedral angle; the gap is also measured and is used to normalize the sensor output so that the height sensitivity is independent of gap.

2.2. (Full) Interaction matrix and Calibration

The A-matrix described in control analyses of segmented primary mirrors[8,10] relates the vector of height and dihedral response y_h at segment edge sensor locations to the vector z of mirror segment displacements at the actuator locations, so $y_h = A_{hz} z$. If the actuators are perfect position actuators, then the matrix can equivalently be described as the sensor response to quasi-static actuator commands. The control algorithm uses this information, together with the difference between actual and desired sensor readings, to determine an estimate $\hat{z}$ of the segment motion (with unobservable global piston, tip, tilt projected out), and then determines the control required to drive the estimated displacement towards zero. A singular value decomposition of A_{hz} has been useful in understanding the properties of this matrix.[8] For realistic choices of dihedral sensitivity, focus-mode is the next smallest singular value after global piston, tip, and tilt. The next least observable modes (relatively large ratio of rms surface motion to resulting rms edge discontinuity[10]) are spatially smooth, and similar to Zernike basis functions.

The full interaction matrix relates all three displacements at the sensor location (height + dihedral, gap, and shear) to all 6 possible rigid-body deflections of each mirror segment. The segment-normal motion z can be described as before by the motion at each of the three actuator locations, while the remaining "in-plane"

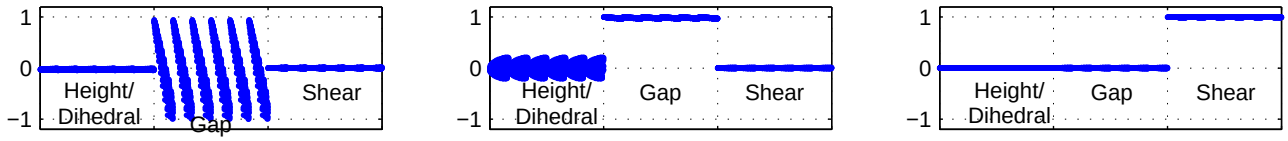

Figure 4. The height (mixed with dihedral), gap, and shear response at sensors (normalized by maximum response) for a few deflection patterns. *Focus-mode* (left), *breathing-mode* (center), corresponding to pure translation of every segment radially along the optical prescription, and *torsion-mode* (right), corresponding to uniform clocking of every segment. Focus-mode also produces a nearly-uniform dihedral signature.

motion w is described by radial and azimuthal translations of the segment along the surface that describes the optical prescription, and the clocking about the segment-center normal. Thus with y_h, y_g, and y_s as the height (combined with dihedral), gap and shear respectively at the sensor locations, then

$$\begin{bmatrix} y_h \\ y_g \\ y_s \end{bmatrix} = \begin{bmatrix} A_{hz} & A_{hw} \\ A_{gz} & A_{gw} \\ A_{sz} & A_{sw} \end{bmatrix} \begin{bmatrix} z \\ w \end{bmatrix} \tag{1}$$

For TMT there are $N = 492$ segments, $n_a = 3N = 1476$ actuators, and $n_s = 2772$ edge-sensor locations, so the full interaction matrix has dimension (2772×3) by (492×6). The subblock $A = A_{hz} \in \mathbb{R}^{n_s \times n_a}$ is the standard A-matrix described earlier. The full interaction matrix has rank $6N - 6$ with unobservable degrees of freedom corresponding to the six rigid-body motions of the primary mirror. For a flat mirror, there is no coupling between in-plane and out-of-plane motion, so $A_{hw} = A_{gz} = A_{sz} = 0$.

The signatures of a few relevant response patterns are shown in Fig. 4 (these do not in general correspond to basis vectors obtained from the singular value decomposition). "Torsion mode", defined as an equal clocking of every segment, produces almost pure shear at the sensor locations, and very little gap. Indeed A_{gw} has rank $n_a - 4$; the three in-plane rigid body motions are unobservable, as is a pattern almost identical to how we have defined torsion mode. Other than the effect of this unobservable mode, the shear at sensor locations can be estimated from the gap measurements through reconstruction of the vector of in-plane motion w as[11]

$$\hat{y}_s = A_{sw}\hat{w} = A_{sw}A_{gw}^{-1}y_g \tag{2}$$

where we use the notation $(\cdot)^{-1}$ to denote the pseudo-inverse. This allows calibration of the sensor response to both gap and shear motion using only gap measurements, with errors due to the unobservable torsion mode, and due to the propagation of gap measurement noise. APS measurements at different zenith angle and temperature are used to compute coefficients of a "fit function" or correction formula for each sensor to determine how the desired set-point should change as a function of the local gap and shear. The calibration modeling software has allowed the comparison of several candidate fit functions, and evaluation of the calibration algorithm performance.

Even with ideal sensors there is a height discontinuity from segment clocking ($A_{hw} \neq 0$). The control algorithm can make this worse in trying to correct the apparent motion; the out-of-plane displacement that results is

$$\hat{z} = A_{hz}^{-1}A_{hw}w \tag{3}$$

This is plotted in Fig. 5 for a representative segment clocking case (the idea for creating this plot comes from H. Bonnet at ESO); this effect will also be minimized with the sensor calibration algorithm (indeed this effect is much smaller than the effect due to installation tolerances). Torsion mode is not observable without shear sensors; it results in M1CS introducing focus-mode, however, the resulting amplitude due to finite element model (FEM) computed in-plane gravity motions is negligible.

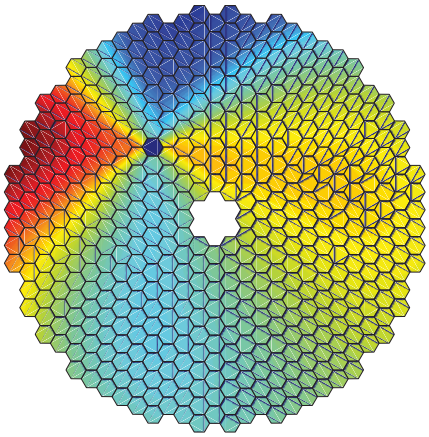

Figure 5. Response pattern that results from the control system cancelling the sensor height readings that result from in-plane clocking of a single segment; the rms surface error is 40 nm/mrad.

2.3. Interaction matrix uncertainty

The condition number of A_{hz} (hereafter denoted A) scales with the number of segments, and thus robustness to small errors has the potential to be a larger challenge for TMT than Keck. The quasi-static modeling code is used to evaluate the variation and uncertainty in A. There are three important sources of uncertainty: (i) errors that affect every non-zero element independently, due to sensor installation tolerances (or due to measurement accuracy if A is measured), (ii) variation in $L_{\rm eff}$ due to variation in gap with zenith angle, temperature, or installation tolerances, and (iii) uncertainty or variation in sensor gain, which we explicitly separate out of A with a diagonal gain matrix $S = I + \delta_S$ as shown in Fig. 6. Uncertain actuator gain has no significant effect on robustness.

The first of the three sources above has been shown to be negligible based on constructing A matrices for various realizations of sensor installation errors; this is not a priori obvious, since extremely small changes in A can lead to instability (of order 1 part in 10^4 if there is no structure to the uncertainty[12]). The second of the three sources may have some effect on dynamic stability as described below, but is easily corrected by using the measured gaps to periodically update A. The final source of uncertainty requires more care to address, even for sensor gain errors of order 1% or less. Note that the A matrix could be measured rather than constructed from geometry, and/or sensor gains could be measured. This could reduce some uncertainty, depending on the measurement accuracy.

Define B_0 as the pseudo-inverse of the nominal (computed or measured) matrix A_0. The control algorithm behaviour depends on the product $Q = B_0SA$; ideally this is identity (except for projecting out global piston/tip/tilt), but will differ for $A \neq A_0$. There are two mechanisms by which A-matrix uncertainty or variability can lead to instability.

First, if Q has an eigenvalue less than zero, then regardless of how small the control bandwidth, the closed-loop system will be unstable. Uncertainty in sensor gain or $L_{\rm eff}$ alone can never lead to this type of instability (barring a sign error); for sensor gain this can be seen from the singular value decomposition $A = U\Sigma V^T$; since $Q = V\Sigma^{-1}U^TSU\Sigma V^T$ will be positive-definite if S is. (The result for $L_{\rm eff}$ variations follows from the dihedral and height sensitivity affecting different modes.[12]) However, this type of instability can occur for errors that affect every non-zero entry of A. This is in principle possible for sensor installation errors, although we have not observed this at realistic tolerances (Table 1). It is certainly possible with uncorrelated measurement errors in A; using

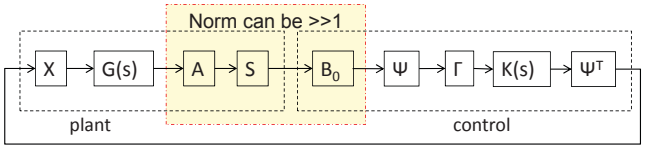

Figure 6. Interaction matrix uncertainty must be considered in conjunction with CSI. The uncertainty in sensor gain $S = I + \delta_s$ and actuator gain $X = I + \delta_x$ are explicitly separated from A. The plant and control dynamics are $G(s)$ and $K(s)$ respectively, with $G(0) = I$. The unitary matrix Ψ transforms into- and out-of a modal basis with diagonal modal gain matrix Γ. Inserting an additional transformation $\Psi^T\Psi$ between $G(s)$ and A allows stability to be proven by considering the norm of $\Gamma\Psi B_0SA\Psi^T$.

Case		$\rho(Q-I)$	$\bar{\sigma}(Q)$	$\bar{\sigma}(\Gamma\Psi Q\Psi^T)$
Zenith	0°	2.5e-3	1.34	1.08
	15°	1.3e-3	1.18	1.04
	25°	0.5e-3	1.06	1.02
	65°	3.8e-3	1.65	1.16
Temp.	−5°	14e-3	1.13	1.02
	+5°	13e-3	1.11	1.02
Segment install error*		10e-3	3.81	1.76
Sensor install error*		6.1e-3	1.91	1.23
Sensor install error†*		4.4e-3	1.24	1.06
Sensor gain*	0.1%	3.9e-3	1.81	1.20
	1%	35e-3	12.6	3.98

Table 1. Effect of variation/uncertainty in A computed by the model due to changes in zenith angle (due to FEA-computed in-plane effects), temperature changes (relative to baseline), installation errors (based on TMT specifications), and sensor gain uncertainty, with the baseline zenith angle of 30°. The metrics plotted are the spectral radius of $Q - I$ indicating how significant the changes in eigenvalues are (stable if < 1), maximum singular value of Q, and the maximum singular value when the focus-mode gain is reduced by a factor of 4. Cases marked * are worst-case over 100 realizations. Case marked with † assumes gap correction.

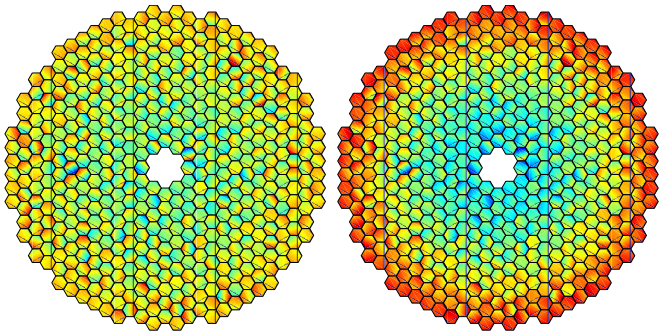

Figure 7. Example of effect of A-matrix uncertainty. For a 0.1% uncertainty in sensor gain case, the pattern on the left results in the estimated pattern on the right (roughly the correct pattern plus 1.7 times focus-mode).

a Monte Carlo analysis then 2% measurement errors give one in 500 risk of instability, and 5% errors greater than a 10% risk.

A more subtle issue is that the maximum singular value $\bar{\sigma}(Q)$ can be large even if the eigenvalues are all stable. While this is not a stability problem in the absence of dynamics, it can lead to performance issues, and more critically, can couple with CSI to result in instability. Large singular values correspond to a large (multi-variable) gain change; to accomodate this requires a large gain margin and a corresponding limit on control bandwidth to guarantee stability. The largest singular value of Q typically corresponds to some high spatial-frequency pattern leading to a correct estimate of that pattern, plus an erroneous and potentially large focus-mode estimate; the particular pattern that has the largest effect depends on the specific errors and is therefore not predictable (an example is shown in Fig. 7, where 0.1% sensor gain uncertainty gives a maximum singular value of 1.7). Instability can occur if driving focus-mode leads to excitation of a structural resonance that also includes some of this particular high spatial-frequency pattern; this in turn would result in a larger erroneous focus-mode estimate and corresponding control system correction, and so forth. While this scenario is unlikely, in order to guarantee stability in the presence of uncertain coupling, we reduce the estimator gain on focus-mode, and constrain the maximum singular value of $(\Gamma\Psi Q\Psi^T)$ where Ψ is a unitary transformation into modal space and Γ a diagonal matrix to reduce the focus-mode gain. This is shown in the final column of Table 1 where focus-mode gain is reduced by a factor of 4; for the example in Fig. 7 the maximum singular value would be reduced to 1.2.

3. DYNAMICS: STRUCTURAL COUPLING

3.1. Structural models

Dynamic analyses for both performance (Sec. 4) and control-structure interaction rely on the finite-element model (FEM) of the telescope structure. In order to provide sufficient detail for the dynamics relevant to M1CS, the structural model of the telescope is divided into an FEM of the main telescope structure, and a detailed FEM of an individual segment assembly. This both allows more detail to be used in the segment model where it is most critical, and allows a single FEM of the telescope structure to be used with different design choices for segment actuators and servo loops; these are integrated into the segment dynamic model as part of the modeling procedure. These two FEMs are then coupled for further analysis, together with disturbances and M1CS control loops, as shown in Fig. 8.

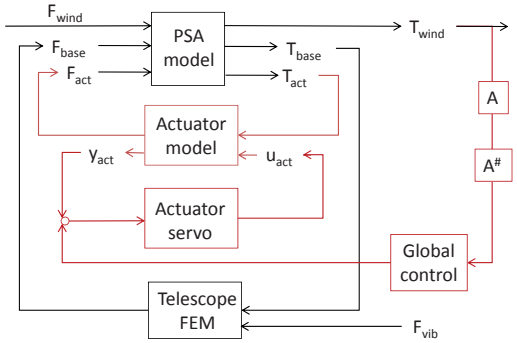

Figure 8. Assembling subsystem models for analysis of control-structure-interaction and dynamic performance. Wind loads are applied to the mirror segment and vibration to the telescope pier. The segment assembly (PSA) is integrated with the telescope FEM, actuator model, and actuator servo loop. Different degrees of fidelity are included as appropriate in performance calculations due to the different frequency requirements.

A modal model is obtained from the FEM of the main telescope structure; 5000 modes (up to nearly 100 Hz; Fig. 9) are typically extracted and ranked based on both their frequency and their projection onto M1 degrees of freedom to evaluate importance, with the static correction retained for truncated modes. For the segment model, a Craig-Bampton model reduction is first performed on the FEM, and because this model is replicated up to 492 times, a simpler lumped-mass model is fit to the transfer functions over the frequency range of interest (below 100 Hz); Fig. 10(b). The segment model has also been experimentally verified (Fig. 10(a)). The two models are coupled by connecting the "matching" nodes of the telescope and segment models, and subtracting the duplicated segment mass from the telescope model. Finally, the actuator model is also fit to experimental data taken from a prototype actuator.[5]

Model validation has been conducted by constructing two fully independent models, one interconnecting the component models in Fig. 8 in state-space, and the other in the frequency domain; both yield identical results for CSI predictions.

3.2. Control-structure interaction

The unsteady forces on the mirror segments due to wind turbulence within the enclosure lead to requirements on the M1CS control bandwidth, of roughly 1 Hz,[3] and also on the low-frequency stiffness of the M1CS actuators, and hence on the servo loop gain. While both the local (actuator servo) and global position control loops would

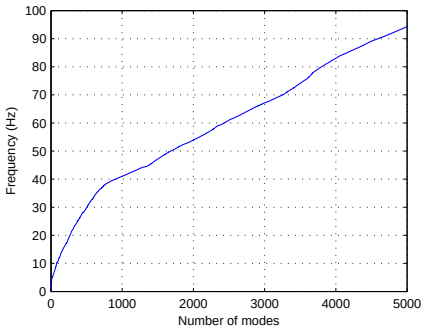

Figure 9. Modal density of main telescope structure; 1000 modes is sufficient for CSI analysis, and 2000 for vibration analysis up to nearly 50 Hz.

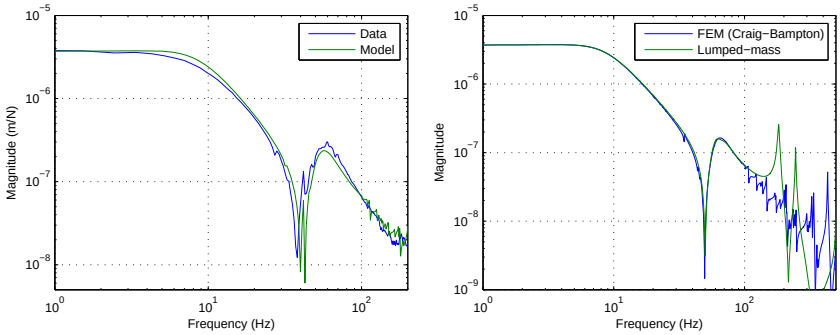

Figure 10. PSA model: (Left) Comparison of experimental and FEM transfer function from actuator force input to actuator encoder output for a segment mounted on a rigid base, and (right) comparison of FEM and lumped-mass approximation (for a 2nd generation, stiffer design).

be straightforward to design if the segments were supported by a rigid backplane, the flexibility of the mirror cell and telescope structure lead to coupling between the segments that can potentially lead to instability. The key insight relevant to analysis is that a diagonal system of identical subsystems is diagonal under any change in basis, and thus the dynamics of the 492 segments and their control can be projected onto a Zernike basis.[13,14] Since the structure is stiff on short length-scales, CSI robustness is only a concern for the lowest spatial frequencies, or equivalently, the lowest Zernike degrees of freedom. Analysis in a Zernike basis is more efficient because results converge with relatively few basis vectors included (Fig. 11(b)). For most analyses, segments are thus "attached" to the telescope FEM in this Zernike basis rather than an individual segment basis, with only the final verification of coupling using all 492 segments. In addition to the rapid convergence in Zernike-space (Fig. 11(b)) that allows for rapid evaluation of models, the Zernike-basis typically nearly diagonalizes the structural dynamics (indeed SISO analysis for each Zernike is a good predictor of the multivariable analysis). This allows a direct correspondance between each peak in the sensitivity and a particular Zernike (e.g. Fig. 11(a)); this information can then be used as a guide to optimizing the telescope structural dynamic characteristics.

Robustness criteria for the actuator servo loop are (i) that the maximum singular value of the sensitivity be less than two at frequencies below ∼15 Hz (the actuator servo block is diagonal, so the sensitivity is the same at the input and output), (ii) collocation and phase stability relied on between 15 and 300 Hz, and (iii) a high gain margin required above 300 Hz. The dynamic model in Fig. 8 is used to evaluate peak sensitivity. For the global control loop, in addition to the peak sensitivity requirement, a principle gain less than 1/2 is required at higher frequencies (equivalent to a gain margin requirement), with an additional factor of two allowance allocated for A-matrix uncertainty.

4. DYNAMIC PERFORMANCE

4.1. Wind

The M1 wind disturbance and response model is described in detail in [3], and will only be briefly summarized here. The basic process is to propagate a pressure-screen across M1, much as a phase screen is used in time-domain adaptive-optics simulations, with forces and moments on each segment computed by integration. This allows the assumed outer-scale to be correctly incorporated, as well as the structural attenuation factor that results from the spatial integration across a segment. This latter effect reduces the high frequency force spectrum relative to the assumed von Karman pressure spectrum and is essential to include to correctly predict the residual wind response after control.

The wind disturbance model is parameterized by the mean wind speed (assumed uniform across the mirror), the rms pressure (also assumed uniform rather than spatially variable), and the outer scale(s) and turbulent energy fraction corresponding to each outer scale; typically we assume that 75% of the pressure has outer scale 5 m (due to vents) and 25% has outer scale 30 m (due to aperture), however, it is important to understand the dependence of performance on all of the parameters.

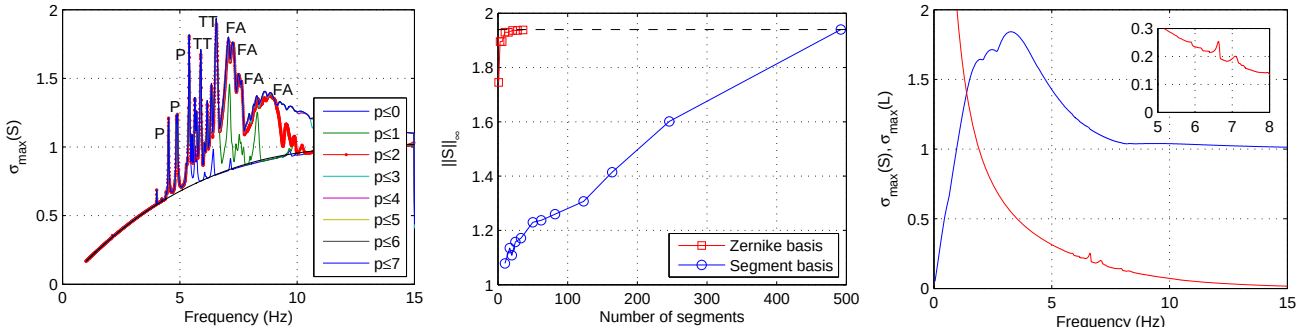

Figure 11. CSI analysis: Maximum singular value as a function of frequency for servo loop (left), for increasing number of basis vectors added by Zernike radial degree p; the legend shows the maximum radial degree included, and the dominant peaks are labeled with "P" if the peak is due to modes that predominantly project onto piston, "TT" if predominantly tip/tilt modes, or "FA" if predominantly focus and astigmatism. The Zernike basis is much more efficient for predicting the maximum over frequency of the largest singular value of the sensitivity, $\|S\|_\infty$ (middle panel). Results converge with relatively few basis vectors, while simply increasing the number of segments in the analysis increases the maximum singular value almost linearly. Global CSI (right) is limited more by constraining the maximum loop gain (red curve) to accomodate interaction-matrix uncertainty than by the maximum sensitivity (blue); the case plotted here corresponds to 1.5 Hz bandwidth on radial degrees 5 and higher, 1 Hz on radial degree 3 and 4, and 0.75 Hz on radial degree 2. The inset shows the principal loop gain, no larger than 0.25 near structural resonances.

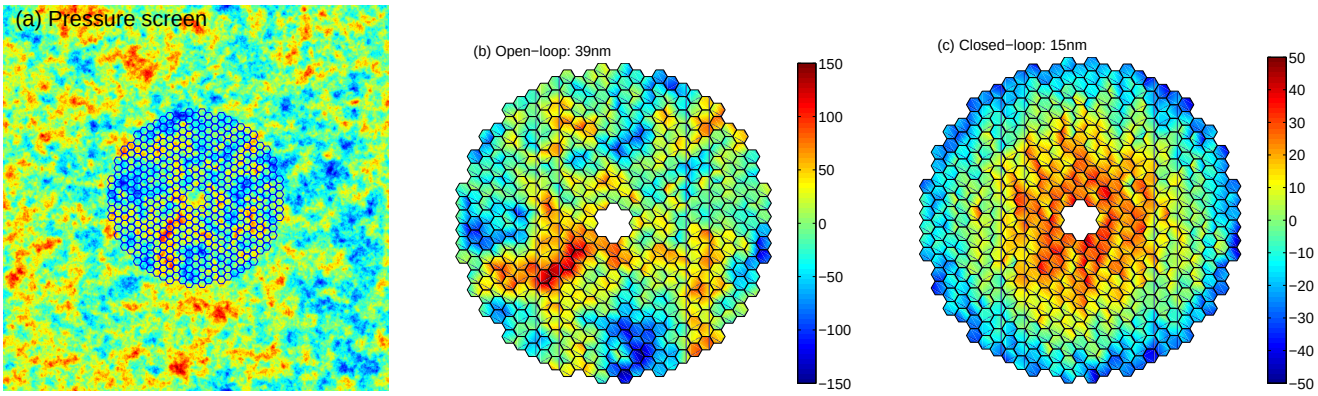

Figure 12. Illustration of wind modeling process, and typical M1 response to 1 m/s wind, in nm, from [2]. Representative pressure screen (left), mirror response without control (center), and with 1 Hz M1CS control bandwidth (right); focus-mode bandwidth here is 0.1 Hz. Global piston, tip and tilt are projected out of the response. The residual rms surface response is 39 and 15 nm rms respectively; in the controlled case, the focus-mode amplitude is 14 nm rms and non-focus-mode residual rms surface response is 6 nm.

Because the wind disturbances are predominantly at very low frequency relative to the telescope structural dynamics, it is computationally more efficient to use a quasi-static telescope structural model rather than propagate wind disturbances across the full dynamic model used for CSI analysis. Similarly, the full dynamics of the segment, actuator, and servo can be fit to the low frequency stiffness behaviour; this depends primarily on the static stiffness and the integral gain of the servo loop (the latter determines how rapidly the compliance increases at low frequencies). The dependence on wind speed, outer scale, and global control bandwidth can be computed and are given in [3].

4.2. Vibration

Equipment vibration can also lead to significant dynamic response for TMT, however, the uncertainty in quantifying the amplitude is much higher than it is for wind. Vibrations can be observed in high resolution measurements at Keck Observatory, including narrowband tones near $\sim 29.6\pm 0.2$ Hz associated with large induction motors as well as tones at lower frequencies attributable to other sources. Most of the wind response is at frequencies well below the AO control bandwidth, so that any motion that is spatially correctable by AO can be corrected.

However, this is not true for equipment vibration, due to the higher temporal frequencies. TMT intends to use best engineering practices on source mitigation; choosing low-vibration equipment, locating vibration sources away from the telescope where practical, and isolating equipment from the foundation; nonetheless there will of course be residual vibration. Of particular concern for the primary mirror is the excitation of segment dynamic resonances. This is a critical challenge for hard actuators with little intrinsic damping, but is largely overcome through the use of soft actuators stiffened with a servo loop.

Because we are interested in the vibration response up to at least 30 Hz and higher, it is essential to include both telescope structural dynamics and the detailed segment, actuator, and servo loop dynamics. The same modeling code used to predict CSI is used to compute the vibration response to vertical input at the telescope pier. (Note that there are many sources of vibration, however the characteristic spatial scale of the response depends on the structural dynamics rather than the source distribution.) Fig. 13 shows the simulated response not just for the baseline soft actuator, but for a representative hard actuator either without or with some passive damping (the damped case is representative of what could be achieved with a tuned shunt circuit on a piezoelectric actuator). Near 29.5 Hz, the hard actuator has more than 2.5 times larger vibration response than the soft, while a hard actuator without any damping can have a response another factor of 5 times worse than the damped hard actuator. Note that both the soft and the damped-hard actuator provide significant damping at higher frequencies; the difference in response between them is partly due to the higher effective damping of the soft actuator, and partly from the lower effective resonant frequency. At low frequencies, all of the actuators perform similarly, as expected.

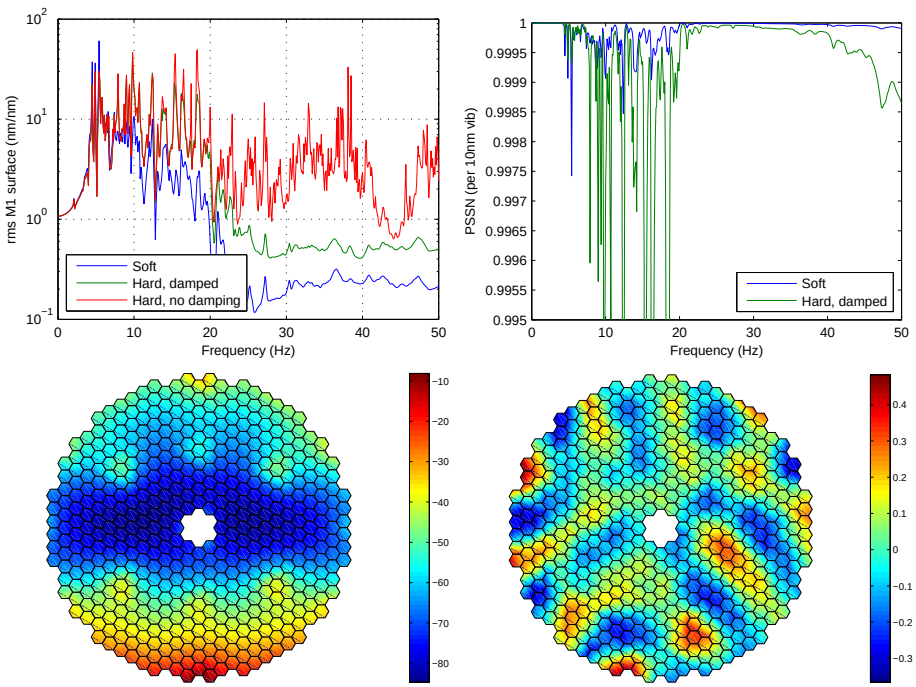

Figure 13. M1 rms surface response (top left, in nm/nm) and corresponding PSSN (top right) in response to vertical pier motion. The PSSN is scaled for a 10 nm pier vibration at each frequency; the full performance estimate involves integrating the product of this response function with the estimated pier vibration. The poor PSSN of the hard actuator without damping is not shown. The soft actuator is the baseline selection for TMT; hard actuators are shown for comparison, both with and without damping (damping parameters chosen from experimentally-validated LR-shunt circuit on a piezoelectric actuator). At higher frequencies the response involves higher spatial-frequencies with worse optical consequences than lower spatial-frequencies of the same rms surface error; response patterns with the soft actuator at the 5 Hz resonance and at 29.6 Hz are shown lower left and right.

Modeling has also been used to explore the parametric dependence of vibration response on the effective segment damping ratio and resonant frequency.[3] Note that when 492 segments are placed on a compliant mirror cell, the coupled resonant frequencies are lower than the rigid-base frequencies, with a spread in resonances.

5. SUMMARY

In order to design and build a high-performance, reliable, yet cost-effective observatory, modeling is absolutely essential. The ability to precisely control the 492 segments of the TMT primary mirror is a key enabling technology for a 30 m-class telescope, and modeling has, and will continue to play an important role in the design and analysis of the primary mirror control system, and ultimately during integration, testing, and monitoring throughout the life of the observatory. Key modeling components include (i) quasi-static tools to simulate and

verify the overall algorithm and to obtain sensor-actuator interaction matrices that include sufficient fidelity to address sensor calibration studies and control system robustness to uncertainty, (ii) dynamic modeling that couples the telescope finite element model, segment models, and actuator models, to predict achievable control system bandwidth for both actuator servo and global edge-sensor feedback in the presence of structural dynamics and interaction matrix uncertainty, and (iii) dynamic models that also include wind and vibration disturbances in order to predict the resulting performance as a function of design parameters.

Acknowledgements

The TMT Project gratefully acknowledges the support of the TMT partner institutions. They are the Association of Canadian Universities for Research in Astronomy (ACURA), the California Institute of Technology and the University of California. This work was supported as well by the Gordon and Betty Moore Foundation, the Canada Foundation for Innovation, the Ontario Ministry of Research and Innovation, the National Research Council of Canada, the Natural Sciences and Engineering Research Council of Canada, the British Columbia Knowledge Development Fund, the Association of Universities for Research in Astronomy (AURA) and the U.S. National Science Foundation.

JCS, LCR, and MMC are employed at the Jet Propulsion Laboratory, California Institute of Technology, which is operated under contract for NASA.

REFERENCES

1. Jared, R. C. *et al.*, "The W. M. Keck Telescope segmented primary mirror active control system," *Proc. SPIE Vol. 1236 Advanced Technology Optical Telescopes IV* (Barr, L. D., ed.), 1990, pp. 996–1008.
2. Aubrun, J.-N., Lorell, K. R., Mast, T. S., and Nelson, J. E., "Dynamic Analysis of the Actively Controlled Segmented Mirror of the W. M. Keck Ten-Meter Telescope," *IEEE Control Systems Magazine*, pp. 3–9, Dec. 1987.
3. MacMynowski, D. G., Colavita, M. M., Skidmore, W., and Vogiatzis, K., "Primary mirror dynamic disturbance models for TMT: Vibration and wind," *Proc. SPIE 7738*, 2010.
4. MacMynowski, D. G., Thompson, P., Shelton, C., and Roberts, Jr., L. C., "Robustness of Thirty Meter Telescope primary mirror control," *Proc. SPIE 7733*, 2010.
5. Thompson, P. M., MacMynowski, D. G., Colavita, M. M., Regehr, M. W., and Sirota, M. J., "Servo design and analysis for the Thirty Meter Telescope primary mirror actuators," *Proc. SPIE 7733*, 2010.
6. Sedghi, B., Müller, M., Dimmler, M., Bauvir, B., Erm, T., Bonnet, H., and Cayrel, M., "Dynamical aspects in control of E-ELT segmented primary mirror (M1)," *Proc., SPIE 7733*, 2010.
7. Troy, M., Chanan, G., Michaels, S., Bartos, R., Bothwell, G., Give'on, A., Hein, R., Radin, M., Roberts, J., Rodgers, J. M., Scherr, L. M., Seo, B.-J., and Zimmerman, D., "A conceptual design for the Thirty Meter Telescope alignment and phasing system," *Proc., SPIE 7012*, 2008.
8. Chanan, G., MacMartin, D. G., Nelson, J., and Mast, T., "Control and Alignment of Segmented-Mirror Telescopes: Matrices, Modes, and Error Propagation," *Applied Optics*, Vol. 43, No. 6, pp. 1223–1232, 2004.
9. Seo, B.-Y., Nissly, C. R., Angeli, G. Z., Ellerbroek, B. L., Nelson, J. E., Sigrist, N., and Troy, M., "Analysis of Normalized Point Source Sensitivity as a performance metric for Large Telescopes," *Applied Optics*, Vol. 48, 2009.
10. MacMartin, D. G. and Chanan, G., "Measurement accuracy in control of segmented-mirror telescopes," *Applied Optics*, Vol. 43, No. 3, pp. 608–615, 2004.
11. Shelton, C., Mast, T., Chanan, G., Nelson, J., Lewis C. Roberts, J., Troy, M., Sirota, M. J., Seo, B.-J., and MacDonald, D. R., "Advances in Edge Sensors for the Thirty Meter Telescope Primary Mirror," *Proc. SPIE 7012*, 2008.
12. MacMynowski, D. G., "Interaction matrix uncertainty in active (and adaptive) optics," *Applied Optics*, Vol. 48, No. 11, pp. 2105–2114, 2009.
13. MacMynowski, D. G., Thompson, P. M., and Sirota, M. J., "Analysis of TMT Primary Mirror Control-Structure Interaction," *Proc. SPIE 7017*, 2008.
14. MacMynowski, D. G., Thompson, P. M., and Sirota, M. J., "Control of many coupled oscillators and application to segmented-mirror telescopes," *AIAA Guidance, Navigation and Control Conference*, 2008.